

# Thrust Characteristics Analysis of Long Primary Double Sided Linear Induction Machine with Plate and Novel Shuttle Secondary Structure

LIU Huijuan\*, ZHANG Qian, MA Jiefang

School of Electrical Engineering, Beijing Jiaotong University, Beijing 100044, P. R. China

(Received 15 May 2019; revised 10 July 2019; accepted 15 August 2019)

**Abstract:** The air-gap flux density formula and thrust expression of long primary double sided linear induction machine (DLIM) in the secondary motion reference frame are deduced by using the Maxwell equations firstly. Then, by analyzing the factors that affect the thrust ripple in the thrust expression, a shuttle type secondary structure of long primary DLIMs is proposed, and its thrust performances of the machine with different shuttle size combinations are simulated and compared with that of plate secondary long primary DLIM. Comparison results show that the new secondary structure can suppress the thrust ripple and improve the stability of system acceleration.

**Key words:** linear induction machine; long primary; ripple; end effect; shuttle secondary

**CLC number:** TM359.4      **Document code:** A      **Article ID:** 1005-1120(2019)05-0693-10

## 0 Introduction

There are many ways to carry out microgravity scientific experiments, such as drop towers, parabolic flights, sounding rockets, space laboratories, space shuttles and international space stations. Among them, the sounding rockets, parabola flights and drop towers are available for micro-gravitational research on earth. The drop towers are the most commonly used facility for microgravity experiments on earth, because of its high level of microgravity ( $10^{-5}g$  or even  $10^{-6}g$ ), low cost, more experimental opportunities and high frequency of use (twice or more experiments per day). However, these facilities increase the operating costs and time intensive<sup>[1-3]</sup>.

For an increase in capacity of test execution and microgravity quality, as well as for the realization of hypo-gravity various, a new drop tower had been designed with a high repetition rate and good accessibility for experiments at low costs by Ref.[1].

In the new drop tower, linear motors (LMs) accelerate the experimental chamber within a certain distance to a definite final velocity, which is determined by the length of microgravity time. Under the same height of the free falling of the experimental chamber, twice the microgravity time can be achieved by the new drop tower system. The new tower can be used as an earthbound facility for conducting large-scale experiments under different gravity conditions such as micro-gravity, hypo-gravity, and hyper-gravity<sup>[2]</sup>.

The movement of the experimental chamber and the setup is shown in Fig.1<sup>[2]</sup>. The chamber is accelerated by LMs from  $0 \text{ m} \cdot \text{s}^{-1}$  to  $v_1 \text{ m} \cdot \text{s}^{-1}$  within  $h_1 \text{ m}$ . And then, the experimental carrier is released and flies autonomously up at a distance of  $(h_2-h_1) \text{ m}$  and down the same height. In the process of free falling, the drive balances the occurring air resistance and keeps the micro-gravity level, approximately  $10^{-6}g$ . Throughout the process, a certain amount of micro-gravity time can be obtained.

\*Corresponding author, E-mail address: hjliu@bjtu.edu.cn.

**How to cite this article:** LIU Huijuan, ZHANG Qian, MA Jiefang. Thrust Characteristics Analysis of Long Primary Double Sided Linear Induction Machine with Plate and Novel Shuttle Secondary Structure[J]. Transactions of Nanjing University of Aeronautics and Astronautics, 2019, 36(5):693-702.

<http://dx.doi.org/10.16356/j.1005-1120.2019.05.001>

After touchdown, the drive and brakes decelerate the experiment chamber to a standstill and prepares for the next test execution<sup>[1-2]</sup>. Experiments are to be performed in microgravity up to 100 times per day by the new drop tower facility which is far more than that by traditional drop tower, several times one day. For vibrational decoupling, two independent structures divide the frame of the system<sup>[2]</sup>.

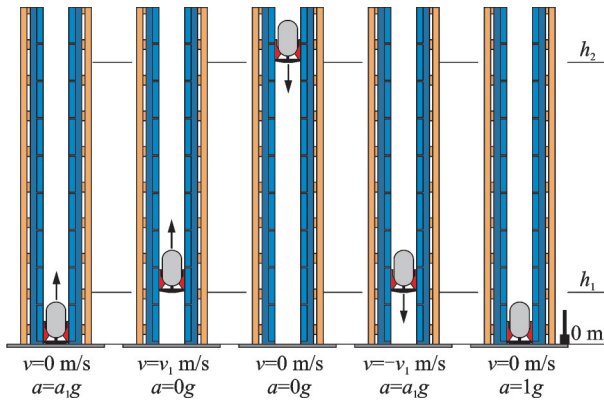


Fig.1 Movement of the experimental setup

Compared with other linear motors, long primary doubly sided linear induction machine (DLIM) is a good candidate to accelerate the experimental chamber because of the lighter mass of the mover, which reduces the thrust requirement of the machine. As other long stator LMs, the finite length secondary of long primary DLIM produces the longitudinal end effect, which consists of forward and backward travelling waves. The forward and back traveling waves of longitudinal end effect not only produce steady thrust force, but also thrust ripple<sup>[4]</sup>. The thrust ripple can be suppressed by control strategy<sup>[5]</sup>, and the longitudinal end effects can also be effectively suppressed by electro-magnetic design<sup>[6-7]</sup>, thereby reducing the thrust ripple of the motor. One method to the reduce thrust ripple is to increase the pole number of the motor, which means the pole pitch decreased when the length of secondary is determined. However, reducing the pole pitch means that the frequency of power supply needs to be increased when the motor velocity is determined. Reducing the slip rate of the motor can also weaken the end effects and reduce the thrust ripple, but the rated current of the motor needs to be increased.

In order to obtain super-high thrust, long primary DLIM with multi-stator structure was proposed<sup>[8-9]</sup>. A slot-less DLIM was presented in Ref.[10], which has improved the power density of the motor. A 12-phase long primary DLIM was proposed in Ref.[11] to solve capacity and system redundancy of power electronic devices.

Generally, the air-gap field expression of long primary DLIM is in the primary moving reference frame, and the thrust is solved by the equivalent circuit considering the end effect<sup>[12-14]</sup>. However, the thrust ripple performance cannot be shown in the equivalent circuit.

The air-gap flux density formula is deduced in the secondary moving reference frame in this paper, and the thrust expression of the plate secondary long primary DLIM considering the end effect is derived, which includes the thrust ripple. The results of finite element calculation are used to show the characteristics of thrust and ripple, and to verify the correctness of analytical calculation expressions. A novel shuttle type secondary for long primary DLIM is proposed, which reduces the mass of the secondary and suppresses the thrust ripple of the motor, on the basis of studying the thrust ripple of plate secondary long primary DLIM.

## 1 Analytical Calculation of DLIMs with Plate Secondary

### 1.1 Air-gap flux density

The longitudinal profile of long primary DLIM with plate secondary is shown in Fig.2.  $g$  is the mechanical air gap length,  $2d$  is the thickness of the secondary,  $\tau$  is the pole pitch, and  $L_2$  is the length of secondary.

Maxwell electromagnetic equations are applied to establish the analytical model of long primary DLIM in the moving reference coordinate of plate

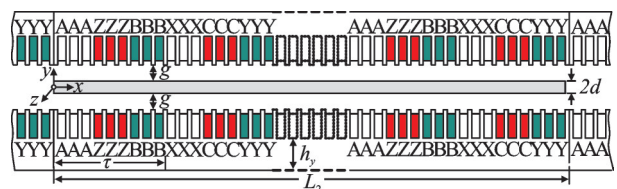


Fig.2 Longitudinal profile of the long primary DLIM

secondary. Although the actual distribution of the field is three-dimensional (3-D), when assuming that all current flows only in the  $z$ -direction and the air gap length is less than a quarter pole pitch, just the  $y$ -component of the air gap field exists. The model becomes 1-D where the  $x$ -component of the field may be ignored<sup>[12]</sup>.

According to the Maxwell equations and the boundary conditions between the coupling zone and the uncoupling zone of the primary and secondary, the air-gap flux density of the coupling and uncoupling zones are derived as

$$\begin{cases} B_{1y} = B_{1y1} + B_{1y2} + B_{1y3} \\ B_{1y1} = B_{1m} \cdot \cos(\omega t + \phi_{1y1}) \\ B_{1y2} = -B_{1m} \cdot sG e^{-\alpha x} \cdot \sin(\omega t + \phi_{1y2}) \\ B_{1y3} = -B_{1m} \cdot sG e^{\alpha(x-L_2)} \cdot \sin(\omega t + \phi_{1y3}) \\ 0 < x < L_2 \end{cases} \quad (1)$$

$$\begin{cases} B_{2y} = -\frac{\mu_0 J_1}{k\delta} \sin(\omega t - kx) & x < 0 \\ B_{3y} = -\frac{\mu_0 J_1}{k\delta} \sin(\omega t - kx) & x > L_2 \end{cases} \quad (2)$$

where  $B_{1y1}$  is the normal travelling wave in the coupling zone ( $0 < x < L_2$ ), which moves at slip speed because the reference coordinate system moves with the secondary.  $B_{1y2}$  is the forward (entry-end) travelling wave, which attenuates along  $x$ -axis and whose attenuation constant is  $1/\alpha$ , and  $B_{1y3}$  is the backward (exit-end) travelling wave, which attenuates along the negative direction of  $x$ -direction and whose attenuation constant is  $1/\alpha$ .  $B_{2y}$  and  $B_{3y}$  are the air gap flux densities of uncoupling region ( $x < 0$  and  $x > L_2$ ), are the same as that of no-load, which move at slip speed.

$$B_{1m} = J_1 \frac{\mu_0}{k\delta} \frac{1}{\sqrt{1 + s^2 G^2}}$$

$$\phi_{1y1} = -kx + \arctan\left(\frac{1}{sG}\right)$$

$$\phi_{1y2} = -\alpha x + \arctan\left(\frac{1}{sG}\right)$$

$$\phi_{1y3} = -kL_2 + \alpha(x - L_2) + \arctan\left(\frac{1}{sG}\right)$$

$$B_{0m} = J_1 \frac{\mu_0}{k\delta}$$

where  $G$  is the goodness factor, and  $B_{0m}$  is the amplitude of no-load air-gap flux density.

$$G = \frac{2\mu_0 \sigma_s f \tau^2}{\pi \delta} \quad (3)$$

$$\sigma_s = \sigma \cdot 2d \quad (4)$$

$$\alpha = \frac{\sqrt{2}}{2} k \sqrt{sG} \quad (5)$$

where  $\sigma_s$  is the effective surface conductivity of the secondary.

### 1.2 Thrust and thrust ripple expressions

The expression of thrust force  $F_e$  including the thrust ripple which considers the forward and backward travelling waves of longitudinal end effect can be calculated by Eq.(6) and the detailed expressions of the thrust and the thrust ripple are derived as Eqs. (7)–(10). In Eq.(6),  $2a$  is the stack thickness of primary core, and  $j_1$  is the surface current density of primary. Different from the short primary linear motor, the length of the secondary of long primary LIM can be any multiple of the primary pole pitch. It can be seen from Eq.(8) that when the length of the secondary plate is integer multiple of the pole pitch, the electromagnetic thrust generated by normal travelling wave does not contain any thrust ripple, and the values of  $F_{e12}$  and  $F_{e13}$  are 0 N for the reason that  $L_2 = 2p\tau$ , where  $p$  is the pole pairs.

In Eq.(9),  $F_{e2}$  is the thrust and thrust ripple produced by the forward travelling wave and  $F_{e3}$  is the thrust and thrust ripple produced by the backward travelling wave. The thrust ripple of long primary DLIMs is only caused by the forward and backward travelling waves when the secondary length is an integral multiple of the pole pitch. From Eqs.(9)–(10), the frequency of the thrust ripple is twice the slip frequency. In addition to producing steady thrust, the forward and backward traveling waves of end effect are the main source of thrust ripple.

The electromagnetic thrust and its ripple generated by forward and backward travelling waves can be expressed by the steady thrust which caused by the normal travelling wave. There is  $\exp(-\alpha L_2)$  in the thrust  $F_{e22}$ ,  $F_{e24}$ ,  $F_{e32}$  and  $F_{e34}$  produced by the end effect, and their values are small.

$$F_e = 2a \int_0^{L_2} \text{Re}(j_1) \text{Re}(B_{1y}) dx \quad (6)$$

$$F_e = F_{e1} + F_{e2} + F_{e3} \quad (7)$$

$$\begin{cases} F_{e1} = F_{e11} + F_{e12} + F_{e13} \\ F_{e11} = K_1 \cdot \frac{L_2}{2} sG \\ F_{e12} = \frac{K_1}{4k} \left[ \cos\left(2s\omega t - \frac{L_2}{\tau} \cdot 2\pi\right) - \cos(2s\omega t) \right] \\ F_{e13} = \frac{K_1}{4k} sG \left[ \sin\left(2s\omega t - \frac{L_2}{\tau} \cdot 2\pi\right) - \sin(2s\omega t) \right] \end{cases} \quad (8)$$

$$\begin{cases} F_{e2} = F_{e21} + F_{e22} + F_{e23} + F_{e24} \\ F_{e21} = -K_2 \sin\left(\arctan \frac{k-\alpha}{\alpha} + \arctan \frac{1}{sG}\right) \\ F_{e22} = K_2 e^{-\alpha L_2} \sin(kL_2 - \alpha L_2 + \arctan \frac{k-\alpha}{\alpha} + \arctan \frac{1}{sG}) \\ F_{e23} = -K_3 \sin(2s\omega t + \arctan \frac{\alpha}{k+\alpha} + \arctan(-sG)) \\ F_{e24} = K_3 e^{-\alpha L_2} \sin(2s\omega t - kL_2 - \alpha L_2 + \arctan \frac{\alpha}{k+\alpha} + \arctan(-sG)) \end{cases} \quad (9)$$

$$\begin{cases} F_{e3} = F_{e31} + F_{e32} + F_{e33} + F_{e34} \\ F_{e31} = -K_3 \sin\left(\arctan \frac{\alpha}{k+\alpha} + \arctan(-sG)\right) \\ F_{e32} = K_3 e^{-\alpha L_2} \sin(-kL_2 - \alpha L_2 + \arctan \frac{\alpha}{k+\alpha} + \arctan(-sG)) \\ F_{e33} = -K_2 \sin(2s\omega t - 2kL_2 + \arctan \frac{k-\alpha}{\alpha} + \arctan \frac{1}{sG}) \\ F_{e34} = K_2 e^{-\alpha L_2} \sin(2s\omega t - kL_2 - \alpha L_2 + \arctan \frac{k-\alpha}{\alpha} + \arctan \frac{1}{sG}) \end{cases} \quad (10)$$

$$\begin{cases} K_1 = 2aJ_1^2 \frac{\mu_0}{k\delta} \frac{1}{1+s^2G^2} \\ K_2 = \frac{1}{2} K_1 sG \frac{\sqrt{1+s^2G^2}}{\sqrt{\alpha^2 + (k-\alpha)^2}} \\ K_3 = \frac{1}{2} K_1 sG \frac{\sqrt{1+s^2G^2}}{\sqrt{\alpha^2 + (k+\alpha)^2}} \end{cases} \quad (11)$$

## 2 Performance Calculation of Plate Secondary Long Primary DLIM

A plate secondary long primary DLIM is designed to verify the accuracy of the analytical expressions, and the specifications for the studied DLIM are summarized in Table 1.

**Table 1 Specifications of the DLIM**

Item	Value
Pole pair	4
Number of slots	48
Pole pitch/mm	66
Slot width/mm	5
Thickness of primary/mm	60
Height of primary/mm	50
Length of secondary/mm	528
Thickness of secondary/mm	4
Mechanical air gap/mm	2
Frequency/Hz	50
Phase current/A	6

### 2.1 Air-gap flux density distribution

The air-gap flux density distribution along the longitudinal direction of plate DLIM under constant current drive ( $I_1=6$  A,  $f_1=50$  Hz) is calculated by the numerical method, and compared with the results by finite element method (FEM), as shown in Fig.3. The longitudinal of air-gap flux density calculated by Eq.(1) has only a few differences compared with the results calculated by FEM. The analytical results have no slot harmonics since slot effect on flux density distribution is considered by Carter's coefficient.

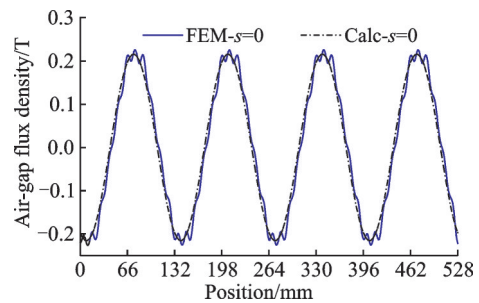


Fig.3 Air-gap flux density distribution

The results of Fourier harmonic decomposition of no-load air-gap flux density calculated by FEM are shown in Fig.4, the main high-order harmonics (11th) of air gap magnetic field is first-order tooth

harmonic. The amplitude of fundamental component calculated by FEM is 0.222 T, and the analytical value of no-load air-gap flux density is 0.216 T. The analytical calculation result is in good agreement with that of the finite element method.

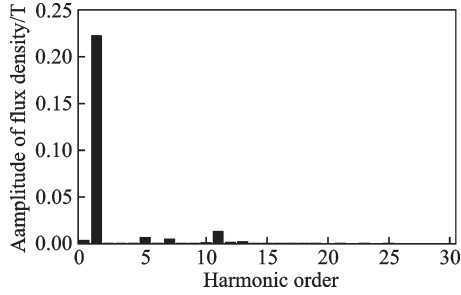


Fig.4 Harmonics of air-gap flux density by FEM

## 2.2 End effect on thrust

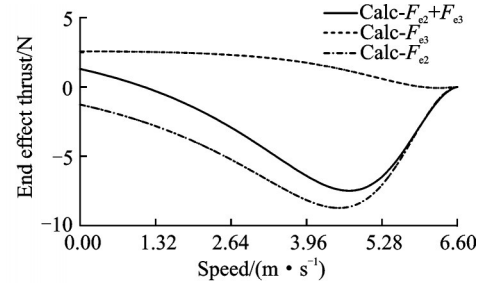
For the conventional plate secondary DLIMs, the length of the secondary is usually  $2p\tau$ , and the values of  $F_{e12}$  and  $F_{e13}$  are 0, according to Eq.(8). The thrust produced by forward travelling wave is composed of four parts, of which  $F_{e21}$  is steady thrust,  $F_{e22}$  is thrust with attenuation coefficient  $\exp(-\alpha L_2)$ ,  $F_{e23}$  is thrust ripple, and  $F_{e24}$  is thrust ripple with attenuation coefficient  $\exp(-\alpha L_2)$ . The thrust generated by backward traveling wave is composed of the same four parts,  $F_{e31}$ ,  $F_{e32}$ ,  $F_{e33}$ , and  $F_{e34}$ .

When the motor is driven by constant current 6 A at rated frequency of 50 Hz, the thrusts produced by forward and backward traveling waves and the end effect thrust are shown in the Fig.5(a). The forward traveling wave thrust is less than 0 N, which is the braking force that hinders the motion of the secondary, and the value of backward traveling wave thrust is greater than 0 N, which increases the thrust of the motor. The thrusts produced by the end effect, including the forward and backward traveling waves, is generally braking force, which increases the motor thrust only at high slip rate, and the braking force is in the stable operation area of the motor. Different from Ref.[15] which considers that the backward travelling wave can be neglected.

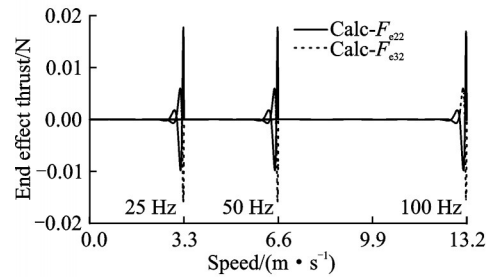
Because  $\exp(-\alpha L_2)$  is close to zero, the thrust  $F_{e22}$  and  $F_{e32}$  with attenuation coefficients are close to zero, as shown in Fig.5(b), whose values are

much smaller than those of steady-state thrust  $F_{e21}$  and  $F_{e31}$ . Similarly, it can be concluded that the values of thrust ripple  $F_{e24}$  and  $F_{e34}$  with attenuation coefficients are approximately equal to 0 N, much less than  $F_{e23}$  and  $F_{e33}$ . Therefore, in motor design and optimization,  $F_{e22}$ ,  $F_{e24}$ ,  $F_{e32}$  and  $F_{e34}$  in Eqs.(9)—(10) can be ignored, for the reason that they have little contribution to the motor thrust, and the expression of thrust can be simplified, compared with Refs.[16-17].

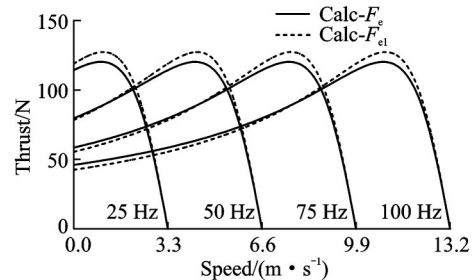
The thrust with and without the forward and backward travelling waves of end effect of the plate DLIM under constant current drive ( $I_1=6$  A) at different frequencies are calculated by Eqs.(8)—(10), as shown in Fig.5(c). The existence of end effect reduces the thrust in the stable operation zone of the motor, and increases the starting thrust at high frequency.



(a) End effect steady thrust



(b) End effect thrust with attenuation coefficient



(c) Thrust-speed characteristic curve

Fig.5 Thrust performance by using analytical method

## 2.3 Verification of thrust and thrust ripple

The calculation results of FEM are used to ver-

ify the correctness of the derivation of analytical expressions Eqs.(8)—(10). Fig.6(a) shows the thrust waveform calculated by the above two methods at the slip rate of 0.15. The frequency of thrust ripple is twice the slip frequency, and the results obtained by the two methods are consistent. The smaller value of the analytical calculation may be due to the consideration of slots effect by the Carter's coefficient.

The thrust-speed characteristics, the thrust ripple-speed characteristics and the ratio of thrust ripple amplitude to thrust of the DLIM at different frequencies calculated by analytical method are verified by FEM, and they are in good agreement, as

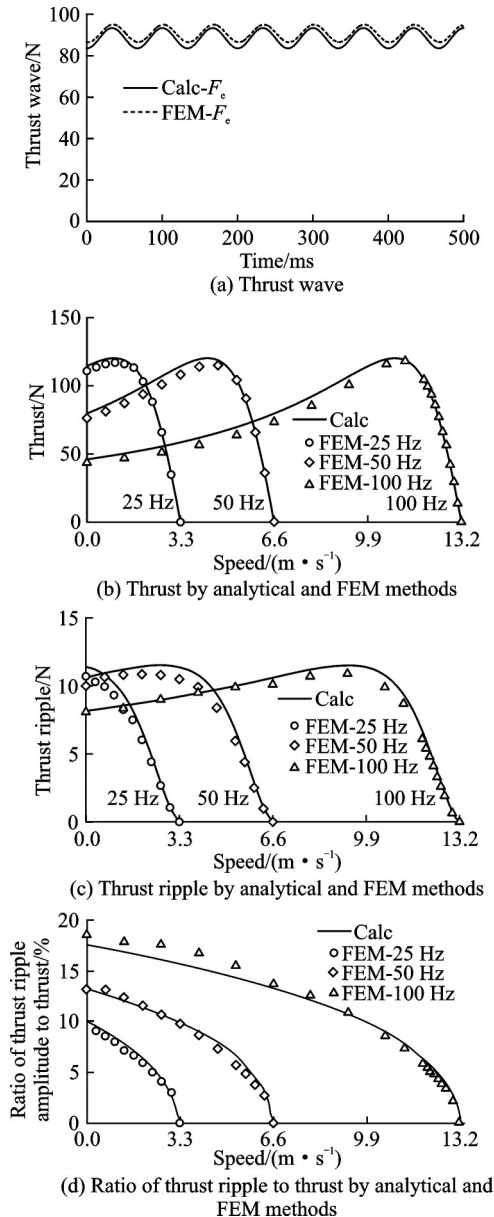


Fig.6 Verification of thrust performance by FEM

shown in Fig.6(b, c, d). The results of FEM calculation confirm the correctness of the formulas deduced in Section 3.1.

### 3 New Shuttle Secondary for Suppressing Thrust Ripple

The expression of the thrust and thrust ripple shows that the thrust ripple of motor is related to the design parameters of motor itself and the slip rate. It can be seen from Fig.6(d) that the ratio of thrust ripple to thrust value of the motor decreases with the increase of speed. Reducing the slip can reduce the ratio of the thrust ripple, but it should be noted from Fig.6(b) that the motor thrust will decrease rapidly. It is of great significance to suppress the output thrust ripple of the DLIMs for improving the gravity level of the microgravity electromagnetic launch system.

The special secondary structure can also effectively restrain the thrust ripple. Eqs.(8)—(10) show that the initial phase of thrust ripple varies when the secondary length is not an integer multiple of the pole pitch. And the ripple of electromagnetic thrust caused by forward travelling wave is only related to the design parameters and the slip rate of the motor, but not to the length of the secondary. A novel shuttle type secondary is proposed, whose exit-end width decreases linearly to suppress the thrust ripple caused by the back travelling wave of the longitudinal end effect at the exit-end, as shown in Fig.7. This new type of secondary can be seen as many different lengths of secondary units superimposed along the  $z$ -axis direction. According to the characteristics of sinusoidal functions, when the secondary unit lengths changes from  $(L_2 - \tau)$  to  $L_2$ , the thrust ripple will produce a phase angle difference of 0 to  $2\pi$  among the secondary units, thus the amplitude of the sinusoidal wave can be reduced and the total thrust ripple can be reduced. In order not to generate lateral force, the tip of shuttle secondary is designed to be symmetrical about the  $xoy$  plane.

Similar conclusions can be drawn from Eqs.(8)—(10) that the thrust ripple can also be reduced when the length of the exit-end  $L_{20}$  is more than one inte-

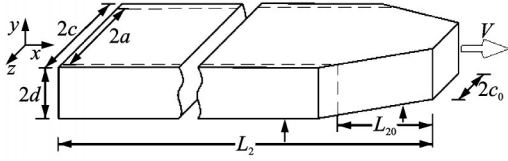


Fig.7 The new type secondary

ger multiple of the pole pitch. Because the phase angle of the thrust ripple is also from 0 to  $2\pi$  among the secondary units, which is the same as the angle range when the tip length is one pole pitch, that is, the secondary unit lengths changes from  $(L_2 - \tau)$  to  $L_2$ .

Since the thrust ripple is composed of four sine functions  $F_{e12}$ ,  $F_{e13}$ ,  $F_{e23}$  and  $F_{e33}$  with the same frequency. According to the periodicity of sine function, different tip lengths may produce the same thrust ripple value. But from Eq.(8), it can be seen that the steady thrust  $F_{e1}$  is positively correlated with the length of the secondary, and the thrust decreases with the increase of the tip length. In order to reduce the steady thrust of the motor as small as possible, the best length of the tip is no more than one pole pitch.

The thrust and thrust ripple of the new secondary motor considering the longitudinal end effect can be calculated by Eq.(12). Because the proposed secondary model is considered as a series of different lengths of secondary units stacked along the  $z$ -axis direction, when the transverse end effect is not considered.

$$F_e = 2c_0 \int_0^{L_2} \text{Re}(j_1) \text{Re}(B_{1y}) dx + 2 \sum_{i=0}^n \frac{a - c_0}{n + 1} \int_0^{L_2 - L_{2i}} \text{Re}(j_1) \text{Re}(B_{1y}^{(i)}) dx \quad (12)$$

where  $B_{1y}^{(i)}$  is the air-gap flux density of the coupling zone when the length of secondary unit is  $(L_2 - L_{2i})$  m.

#### 4 Comparison of Thrust Performance between Shuttle and Conventional Secondary

From Section 2, it can be seen that the thrust ripple of the plate secondary DLIM is obvious, the

ratio of ripple to thrust is about 8.3% at maximum thrust value, which affects the stability of acceleration of microgravity experimental chamber launch system. The FEM is employed to compute the thrust and thrust ripple characteristics of DLIM with new shuttle secondary and compared with that of plate secondary DLIM.

##### 4.1 Effect of the shuttle size on thrust

When the mover is the shuttle type, the thrust is smaller than that of plate type, and the length and width of shuttle tip in Fig.8(a) are 66 mm and 0 mm, respectively. Fig.8(b) shows the thrust with different exit-end width  $2c_0$  and the length of tip  $L_{20}$  of the shuttle type secondary. Where the width  $2c_0 = 60$  mm or the length  $L_{20} = 0$  is the plate secondary. The thrust decreases with the increase of the length  $L_{20}$  when the exit-end width  $2c_0$  of the shuttle is constant, which is the same as decreasing the exit end width of the shuttle by keeping its length unchanged. The electromagnetic thrust decreases the most when the length is maximum and the width of the secondary end is minimum, 0 mm. As can be seen from the contour line in Fig.8(b), it can be seen that different combinations of the length  $L_{20}$  and width  $2c_0$  can be selected for the same thrust value.

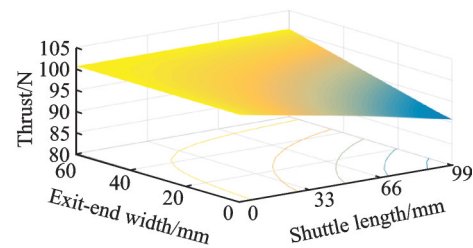
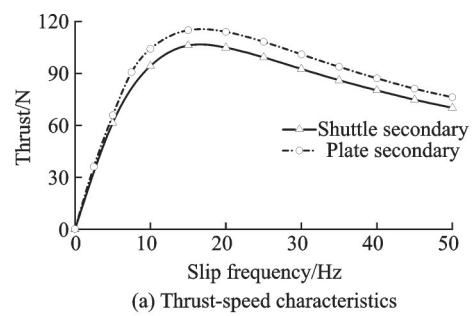


Fig.8 Thrust characteristics

##### 4.2 Thrust ripple of shuttle DLIM

The thrust ripple distribution with the length

and end width of the shuttle is shown in Fig.9 when the slip rate is 0.2. It appears that the thrust ripple is obviously suppressed when the secondary is the shuttle type, especially when the end width  $2c_0$  is less than 20 mm and the tip length  $L_{20}$  is more than 33 mm, where the shuttle tip length  $L_{20}=0$  mm or the exit-end width  $2c_0=60$  mm is the plate secondary.

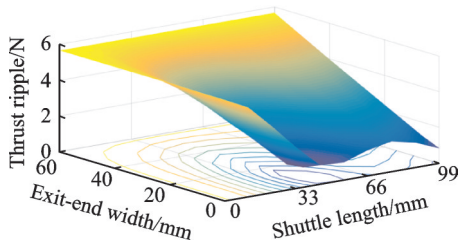


Fig.9 Thrust ripple distribution

When the exit-end width of the shuttle is close to that of the plate secondary, the peak value of thrust ripple decreases with the increase of the shuttle tip length, but the suppression of the thrust ripple is very limited. Similarly, when the tip length of the shuttle is close to 0 mm, the suppression of thrust ripple is also limited with the decrease of the shuttle exit-end width. Reducing the exit-end width and increasing the tip length at the same time can quickly reduce the peak value of thrust ripple. The minimum thrust ripple can be obtained in regions where the length  $L_{20}$  is from 33 mm to 66 mm ( $1\tau$ ) and the width  $2c_0$  is less than 20 mm. Because the forward traveling wave produces a certain phase thrust ripple, the minimum value of the resultant thrust ripple is obtained when the shuttle length is less than one pole pitch (66 mm). The different combinations of the length  $L_{20}$  and width  $2c_0$  can be selected for the same thrust ripple, as shown in Fig.9.

#### 4.3 Thrust density distribution

When the shuttle tip length is greater than one pole pitch, and the exit-end width of the secondary is close to 0 mm, the thrust ripple ( $F_p$ ) can also be effectively reduced, although the minimum value cannot be obtained. Nevertheless, it can be seen from Fig.8 and Fig.10 that the thrusts of the motor and the thrust density (thrust per secondary mass)

are decreased, thus the tip length of the shuttle secondary greater than one pole pitch is not the optimal choice.

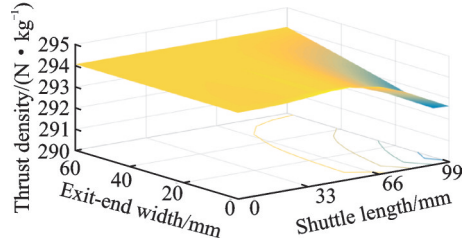


Fig.10 Thrust density distribution

Therefore, the shuttle length  $L_{20}$  and exit-end width  $2c_0$  can be selected in combination with the thrust, thrust ripple and thrust density distribution, so that the thrust reduction is not much and the thrust ripple can be well suppressed, while the thrust density changes little.

When the secondary is the plate type, the maximum thrust is obtained, but the thrust ripple is also much larger, compared with that of the shuttle secondary, and the ratio of thrust ripple to thrust is up to 5.63% at the slip 0.2. The thrust, thrust ripple and thrust density are shown in Table 2, when the tip length and width of the new shuttle secondary are different combinations, when the tip length  $L_{20}=0$  mm is the plate secondary. When the length and width are 44 mm and 12 mm, respectively, the thrust of the motor decreases by about 3.3 N, while the ratio of thrust ripple to thrust is only 0.6%, which decreases by 5%. While the thrust density remains unchanged due to reduction of the new type secondary mass.

**Table 2 Comparison of performance at different shuttle length and exit-end width**

$L_{20}/$ mm	$2c_0/$ mm	$F_c/$ N	$F_p/$ N	$(F_p/F_c)/$ %	$(F_c/m)/$ (N·kg <sup>-1</sup> )
0		100.61	5.66	5.63	294.10
33	12	98.09	2.08	2.12	294.05
44	6	96.85	0.67	0.69	294.09
44	12	97.27	0.55	0.57	294.09
44	18	97.68	1.08	1.11	294.09
55	0	95.45	0.99	1.04	294.32
55	6	95.89	0.90	0.94	294.05
66	0	94.35	1.43	1.52	294.13
77	0	93.16	1.69	1.81	293.17

## 5 Conclusions

A shuttle type secondary structure which can effectively suppress the thrust ripple of long primary DLIMs used in microgravity experimental chamber launch system is proposed. Its thrust performances of the machine with different shuttle size combinations are simulated and compared with that of plate secondary long primary DLIM.

(1) When the plate secondary length of the long primary DLIM is not integral multiple pole pitch, the thrust ripple of twice slip frequency will be produced by the normal travelling wave. Both the forward travelling wave and backward travelling wave of longitudinal end effect produce the thrust ripple of twice slip frequency. Longitudinal end effect not only produces the thrust ripple, but also produces stable electromagnetic thrust. The thrust generated by end effect is braking force in stable operation area.

(2) The accuracy of the analytical calculation method is verified by the finite element method, which provides a theoretical basis for the design and optimization of the long primary DLIMs.

(3) The proposed new shuttle secondary can effectively suppress the thrust ripple of the long primary DLIMs for microgravity experimental chamber launch system. Although the thrust of motor decreases, compared with the plate long primary DLIMs, the thrust density remains unchanged.

## References

- [1] LOTZ C, FROBOSE T, WANNER A, OVERMEYER L, et al. Einstein-elevator: A new facility for research from  $\mu\text{g}$  to 5 g[J]. *Gravitational and Space Research*, 2017, 5(2): 11-27.
- [2] LOTZ C, WESSARGES Y, HERMSDORF J, et al. Novel active driven drop tower facility for microgravity experiments investigating production technologies on the example of substrate-free additive manufacturing[J]. *Advances in Space Research*, 2018, 61(8): 1967-1974.
- [3] THORBEN K, ULRICH K, ANDREAS G, et al. Concept for a next-generation drop tower system[J]. *Advances in Space Research*, 2015, 55(6): 1728-1733.
- [4] LONG X L. Theory and method of electromagnetic design for linear induction Motors[M]. Beijing: Science Press, 2006.
- [5] SUN X, SHI L M, ZHANG Z H, et al. The thrust fluctuation suppression of segmented double sided linear induction motor[C]// Annual Conference of the IEEE Industrial Electronics Society. Beijing: IEEE, 2017: 3693-3697.
- [6] YANG T, ZHOU L B. Longitudinal dynamic end effect in long primary double-sided linear induction motor Part 1: Airgap magnetic field[J]. *Electric Machines and Control*, 2014, 18(4): 52-59.
- [7] YANG T, ZHOU L B, LI L R. Influence of design parameters on end effect in long primary double-sided linear induction motor[J]. *IEEE Transactions on Plasma Science*, 2011, 39(1): 192-197.
- [8] ZHANG Y X, MA M Z, MA W M, et al. Analysis of saturation characteristics of double-stator linear induction motors[J]. *Proceedings of the CSEE*, 2012, 32(36): 102-108.
- [9] XU J, MA W M, LU J Y. Mathematical model and performance analysis of a four-stator double-sided linear induction motor[J]. *Transactions of China Electrotechnical Society*, 2011, 26(9): 5-12.
- [10] XU J, NIE S X, MA W M, et al. Magnetic circuit calculation of slot-less double-sided long primary linear induction motor[J]. *Proceedings of the CSEE*, 2016, 36(10): 2793-2799.
- [11] RAO J, LIU D Z, XU J, et al. Analysis of mathematical model for long-primary short-secondary twelve-phase linear induction motor[J]. *Journal of Naval University of Engineering*, 2014, 26(2): 10-14.
- [12] YANG T, ZHOU L B, LI L R. Performance calculation for double-sided linear induction motor with short secondary[C]// International Conference on Electrical Machines & Systems. Wuhan: IEEE, 2008: 3478-3483.
- [13] YANG T, ZHOU L B. Longitudinal dynamic end effect in long primary double-sided linear induction motor Part 2: Performance calculation[J]. *Electric Machines & Control*, 2014, 18(8): 67-74.
- [14] LU J Y, MA W M. Research on end effect of linear induction machine for high-speed industrial transportation[J]. *IEEE Transactions on Plasma Science*, 2011, 39(1): 116-120.
- [15] NIE S X, MA W M, LI W C, et al. Research on thrust ripple of long primary linear induction motors with symmetrical current excited[J]. *Proceedings of*

the CSEE, 2015, 35(21): 5585-5591.

- [16] BOLDEA I. Linear electric machine, drives, and MAGLEVs handbook[M]. London, UK: CRC Press, 2013.
- [17] GIERAS J F. Linear induction drives[M]. Oxford, UK: Clarendon, 1994.

**Acknowledgement** This work was supported by the Research Project of Electromagnetic Simulation Research and Development of Induction Motor of Beijing Jiaotong University (No.E18L00100).

**Authors** Prof. LIU Huijuan received Ph. D. in Electrical Engineering from Beijing Jiaotong University in 2009 and received the B.S. degree and M.S. degree from Tianjin University in 1989 and 1994 respectively. She worked as a visiting scholar in the Laboratory for Power Electronics & Electrical Machines, The Ohio State University, Columbus, OH, USA, in 2008. In 2011 and 2013, She worked as a Research Fellow in The Hong Kong Polytechnic University. Since December 2015, she has been a Professor with Beijing Jiaotong University. Her current research interests mainly focus on numerical methods of electromagnetic field computation, optimal design and control of high performance electrical machines and novel electrical motors, such as induction ma-

chine, doubly fed brushless machine, and permanent magnetic machine for wind power and other new power source development.

Mr. ZHANG Qian is a Ph.D. candidate in Electrical Engineering, Beijing Jiaotong University in 2017. His research interest includes the optimal design and analysis of novel permanent-magnet motors, linear induction machines and hardware design of motor drive.

Ms. MA Jiefang is a master degree candidate in Electrical Engineering, Beijing Jiaotong University. Her research interest includes the optimal design and analysis of linear induction machines.

**Author contributions** Prof. LIU Huijuan designed the study, theoretical feasibility analysis the model, conducted the analysis, interpreted the results and wrote the manuscript. Mr. ZHANG Qian contributed data and FEM simulation results for the linear induction motor model, some formulas are deduced and the calculation program is compiled. Ms. MA Jiefang contributed some FEM simulation results. All authors commented on the manuscript draft and approved the submission.

**Competing interests** The authors declare no competing interests.

(Production Editor: Sun Jing)